Suppression of indirect exchange and symmetry breaking in the antiferromagnetic metal HoB_{12} with dynamic charge stripes

K. Krasikov,[1] V. Glushkov,[1] S. Demishev,[1,2] A. Khoroshilov,[1] A. Bogach,[1] V. Voronov,[1] N. Shitsevalova,[3] V. Filipov,[3] S. Gabáni,[4] K. Flachbart,[4] K. Siemensmeyer,[5] and N. Sluchanko[1]

[1]*Prokhorov General Physics Institute of Russian Academy of Sciences, Vavilov str. 38, Moscow 119991, Russia*
[2]*National Research University Higher School of Economics, Myasnitskaya str., 20, Moscow 101000, Russia*
[3]*Frantsevich Institute for Problems of Materials Science, National Academy of Sciences of Ukraine, 03680 Kyiv, Ukraine*
[4]*Institute of Experimental Physics, Slovak Academy of Sciences, Watsonova 47, 04001 Košice, Slovakia*
[5]*Helmholtz Zentrum Berlin, Hahn Meitner Platz 1, D 14089, Berlin*

(Received 23 April 2020; revised 19 October 2020; accepted 1 December 2020; published 28 December 2020)

Precise angle-resolved magnetoresistance (ARM) measurements are applied to reveal the origin of symmetry lowering in electron transport and the emergence of a huge number of magnetic phases in the ground state of the antiferromagnetic metal HoB_{12} with *fcc* crystal structure. By analyzing the polar H-θ-φ magnetic phase diagrams of this compound reconstructed from the experimental ARM data, we argue that nonequilibrium electron density oscillations (dynamic charge stripes) are responsible for the suppression of the indirect Ruderman-Kittel-Kasuya-Yosida exchange along the ⟨110⟩ directions between the nearest neighboring magnetic moments of Ho^{3+} ions in this strongly correlated electron system.

DOI: 10.1103/PhysRevB.102.214435

I. INTRODUCTION

The concurrence between different simultaneously active charge, spin, lattice, and orbital interactions is believed to play a key role in the formation of a rich variety of magnetic structures in phase diagrams of strongly correlated electron systems (SCES) [1]. A well-known example are the manganites with colossal magnetoresistance that demonstrate an enormous number of different states including ferro- and antiferromagnetic (AF) long-range ordering, magnetic short-range correlations, charge and spin density waves, and diversity of structural transitions [1–3]. In the family of cuprates, the competition of high temperature superconductivity with AF ordering is complemented by spin and charge ordering, pseudogap states, and the unusual "strange metal" phase with non-Fermi-liquid behavior at intermediate temperatures [4–6]. Very complicated phase diagrams have been also found in ruthenates [7], organic charge-transfer salts [8], superconducting iron-based pnictides and chalcogenides [9,10], and in Ce-based heavy fermion metals [11], where electron nematic phases were detected. The contention of various states leads often to nanoscale phase separation and spatially inhomogeneous phases that is extremely useful for practical applications due to giant responses to weak enough external perturbations. Unfortunately, the common features of the effects arising in most of these SCES cannot be easily analyzed since these compounds possess a complex chemical composition with a low symmetry crystal structure.

It was recently demonstrated that $Ho_xLu_{1-x}B_{12}$ dodecaborides with a face-centered-cubic (*fcc*) crystal structure may be treated as model SCES, which show electronic phase separation [dynamic charge stripes along the ⟨110⟩ axis, Fig. 1(a)] in combination with dynamic Jahn-Teller instability and a frustrated AF ground state with Néel temperature $T_N \leqslant 7.4$ K [12–15]. In these compounds, the competition between Ruderman-Kittel-Kasuya-Yosida (RKKY) oscillations of the electron spin density [indirect exchange interaction, Fig. 1(b)] and quantum oscillations of the electron density (dynamic charge stripes) is shown to result in an extremely complicated and anisotropic magnetic phase diagram, which has a form of Maltese cross with a huge number of various magnetic phases [14–16]. Since the arrangement of magnetic phases depends dramatically both on the magnitude and direction of external magnetic field, high precision studies of charge transport were performed here to reconstruct the three-dimensional (3D) H-φ-θ magnetic phase diagram of HoB_{12}. As a result, we argue that nonequilibrium electron density oscillations (stripes) seem to be responsible for the suppression of the indirect exchange interaction along the ⟨110⟩ directions and lead to symmetry breaking in this strongly correlated electron system.

II. RESULTS AND DISCUSSION

Detailed studies of heat capacity, magnetization, and magnetoresistance were performed on high-quality single-domain and isotopically enriched (^{11}B) single crystals of $Ho^{11}B_{12}$ ($T_N \approx 7.4$ K). The related experimental details are shown in the Supplemental Material [17]. The H-T magnetic phase diagrams were reconstructed for three principal directions $\boldsymbol{H}||[100]$, $\boldsymbol{H}||[110]$, and $\boldsymbol{H}||[111]$ displaying numerous magnetic phases and phase transitions [Figs. 1(c)–1(e)]. It is worth noting that in contrast to the nearly isotropic AF-P transition (P is the paramagnetic state) in the H-T diagram, the location

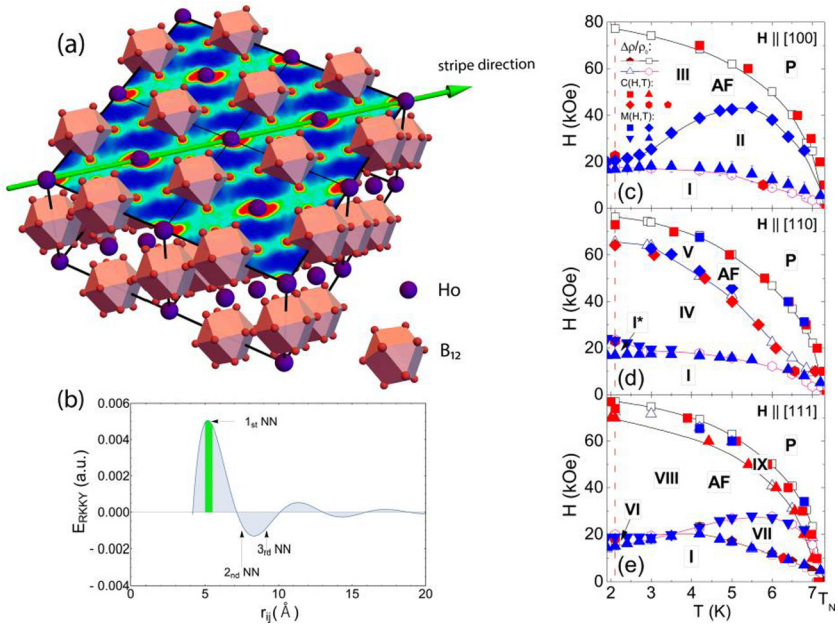

FIG. 1. (a) Crystal structure of RB_{12}. The color plane shows the distribution of the electron density in the dynamic charge stripes (green bands) along with [110] direction [12]. (b) RKKY exchange interaction function in RB_{12}. The vertical green band marks the distance where the dynamic charge stripes destroy the indirect magnetic exchange. Arrows show the position of first (1_{st}NN), second (2_{nd}NN) and third (3_{rd}NN) nearest neighbor magnetic ions in the *fcc* lattice. (c)–(e) *H-T* magnetic phase diagrams of $Ho^{11}B_{12}$ obtained from magnetoresistance $\Delta\rho/\rho_0$, heat capacity $C(T, H)$ and magnetization $M(T, H)$ measurements [see legend in panel (c)] for three principal directions $H\|[100]$, $H\|[110]$, and $H\|[111]$ [panels (c), (d), and (e), respectively]. Roman numerals indicate different AF phases, P denotes the paramagnetic state. The red dotted vertical line indicates the temperature $T = 2.1$ K where the measurements leading to the 3*D* (H-φ-θ) diagram were performed.

of phase boundaries inside the AF phase is considerably different for various $\boldsymbol{H}$ directions [Figs. 1(c)–1(e)]. The results of our precise measurements allowed us to refine the *H-T* diagrams detected previously in Refs. [16,18,19]. Besides, we show below that despite the high symmetry of the crystal lattice are *the magnetic phases for the principal field directions* separated by radial phase boundaries and, hence, these phases *are completely different,* and that only one low-field AF state (marked as I in Fig. 1) exists for any magnetic field orientation.

To clarify the location of phase boundaries in the AF state in external magnetic field up to 80 kOe, angle-resolved magnetoresistance (ARM) was investigated at fixed temperature T = 2.1 K [see vertical dotted line in Figs. 1(c)–1(e)] in four experiments with sample rotating around excitation current directions (i) $\boldsymbol{I}\|[100]$, (ii) $\boldsymbol{I}\|[1\bar{1}0]$, (iii) $\boldsymbol{I}\|[111]$, and (iv) $\boldsymbol{I}\|[112]$. For example, the experimental data obtained with rotating around $\boldsymbol{I}\|[100]$ [see case (i) above] are presented in Fig. 2. Results of these experiments may be summarized as follows. Firstly, only a slight cosine-like $\rho(\varphi) \sim \cos(2\varphi)$ modulation is detected when the magnitude of H does not exceed ~20 kOe [the phase boundary position, which restricts the "I" phase, see Figs. 1(c)–1(e)]. Secondly, the increase of magnetic field above ~25 kOe leads to two additional features (sharp peaks in the neighborhood of ⟨110⟩ directions and "horns" that are symmetrical to the ⟨100⟩ axis) appear and become broader with $\boldsymbol{H}$ increase. Thirdly, the cosine-like behavior is restored above the Néel field ($H_N \sim 76$ kOe) with two additional features, different from the low-field data: (a) the phase of cosine is shifted by 45 degrees and (b) a narrow local minimum of tiny amplitude appears near the ⟨001⟩ direction.

It is worth noting that abrupt anomalies in the AF phase observed in the wide neighborhood of ⟨100⟩ directions may be associated with magnetic phase transitions between states with different magnetic order [13,14]. Besides, the unusual behavior of sharp peaks in the vicinity of ⟨110⟩ directions is suggested to be induced by the dynamic charge stripes along ⟨110⟩ axis [see Fig. 1(a)].

The same features can be easily resolved on magnetic field dependences of resistivity measured at the same configura-

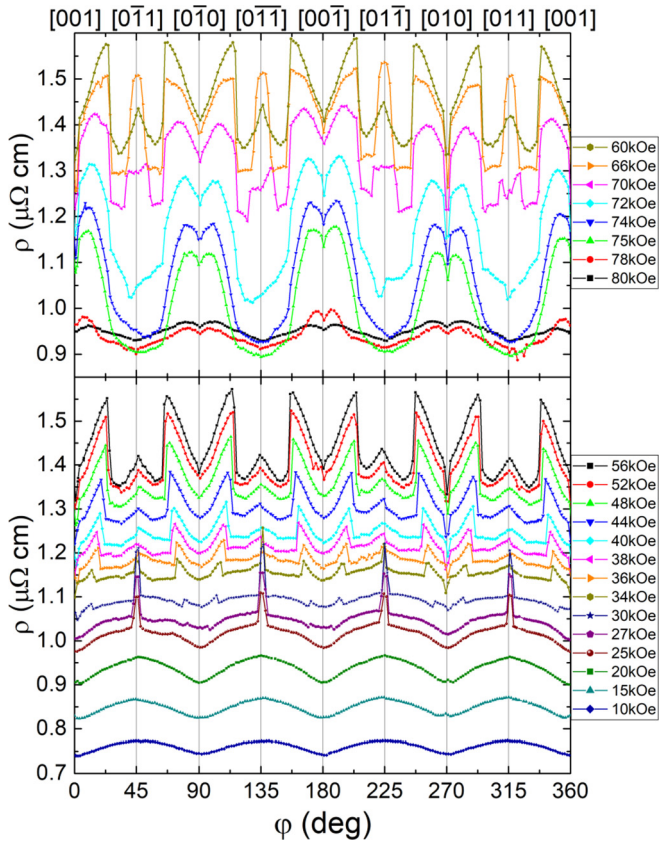

FIG. 2. Angular dependences of $Ho^{11}B_{12}$ resistivity for the various magnetic field at $T = 2.1$ K. The rotation was performed around the axis $I\|[100]$. Vertical lines indicate the positions when the magnetic field H is aligned with principal axes.

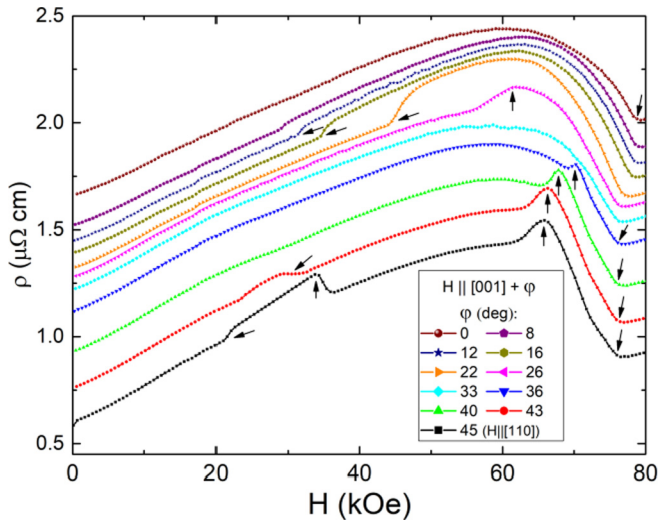

FIG. 3. Magnetic field dependences of the $Ho^{11}B_{12}$ resistivity at $T = 2.1$ K for different angles $\varphi = (n, H)$ between the normal to the sample $n\|[001]$ and magnetic field H. Arrows indicate the orientational magnetic phase transitions. The rotation was performed around the axis $I\|[100]$. Curves are shifted for convenience.

tion $\boldsymbol{I}\|[100]$ for a set of different $\boldsymbol{H}$ directions (Fig. 3). For example, the data for $\boldsymbol{I}\|[100]$ unambiguously evidence that (1) varying of the angle $\varphi = (\boldsymbol{n}, \boldsymbol{H})$ between the normal to the sample surface $\boldsymbol{n}||[010]$ and the applied magnetic field $\boldsymbol{H}$ allows one to detect a set of anomalies on $\rho(H, \varphi_0)$ curves, which may be attributed to orientation magnetic transitions. Besides, it is seen that (2) positive magnetoresistance dominates in the AF phase up to the sharp drop just before the Néel field. It is important to note also that a wide hump appears in the range of $H = 22 - 35$ kOe in the proximity ($\Delta\varphi = 2 - 3^\circ$) of [110] direction when a magnetic field is applied along the dynamic charge stripes (see Fig. 3). Similar data sets have been collected in our experiments with sample rotation around current directions (ii) $\boldsymbol{I}\|[1\bar{1}0]$, (iii) $\boldsymbol{I}\|[111]$, and (iv) $\boldsymbol{I}\|[112]$ (see Figs. S4–S7 in Ref. [17]). The overview of both the magnetic phases and phase transitions inside the AF state of $Ho^{11}B_{12}$ on the basis of our experiments is provided below.

The processed ARM data for all (i)–(iv) sample rotation experiments can be easily displayed in the polar presentation $\Delta\rho/\rho = f(H, \varphi)$. Figure 4 shows the polar plot of the magnetoresistance (MR) results at T = 2.1 K obtained in experiments (i) (panel (a), rotation axes $\boldsymbol{I}\|[100]$) and (ii) (panel (b), $\boldsymbol{I}\|[1\bar{1}0]$) together with their projection on the (100) and $(1\bar{1}0)$ planes (panels (c) and (d), respectively). Two other sets of the ARM data and the diagrams for (iii) $\boldsymbol{I}\|[111]$ and (iv) $\boldsymbol{I}\|[112]$ rotation axes are presented in Fig. 5. The phase boundaries on H-φ plane diagrams [open symbols in Figs. 4(c) and 4(d) and Figs. 5(c) and 5(d) are related to sharp features detected on the $\Delta\rho/\rho$ angular dependences and MR derivatives $d\rho/dH$ (see Ref. [17] for more detail). It is worth noting that the rotation around the $\boldsymbol{I}\|[1\bar{1}0]$ axis enables one to obtain in one experiment the transverse MR variation when the direction of magnetic field changes step-by-step between three principal axes in the *fcc* lattice ($\boldsymbol{H}\|[001]$, $\boldsymbol{H}\|[110]$, and $\boldsymbol{H}\|[111]$). Several regions corresponding to phases with different magnetic ordering can be easily resolved in Figs. 4(b) and 4(d). The obtained H-φ diagram [Fig. 4(d)] appears to be crucial for further understanding of the structure of the polar H-φ-θ phase diagrams. Similar "Maltese Cross" anisotropy in the $(1\bar{1}0)$ plane was found recently [15] in a related $Ho_{0.8}Lu_{0.2}B_{12}$ system. Such a type of MR anisotropy is constructed from four principal regions that can be easily distinguished in Fig. 4(d): (1) the central circularlike region

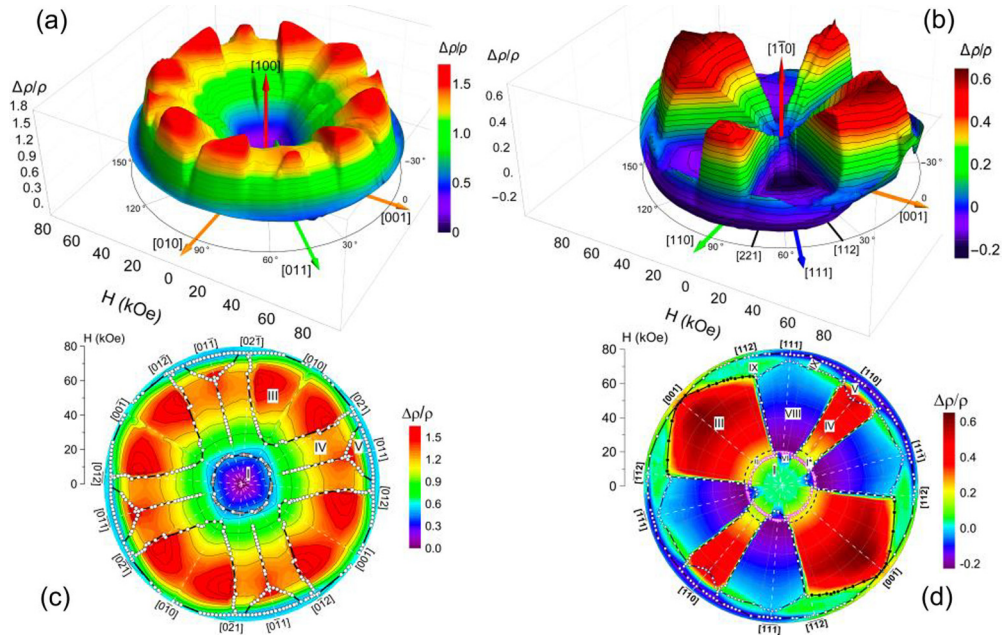

FIG. 4. Magnetoresistance $\Delta\rho/\rho = f(H, \varphi)$ of $Ho^{11}B_{12}$ in cylindrical coordinates for current directions $I\|[100]$ (a) and $I\|[1\bar{1}0]$ (b) and its projection onto (100) and $(1\bar{1}0)$ planes (c) and (d), respectively at $T = 2.1$ K. Roman numerals show different magnetic phases in the AF state.

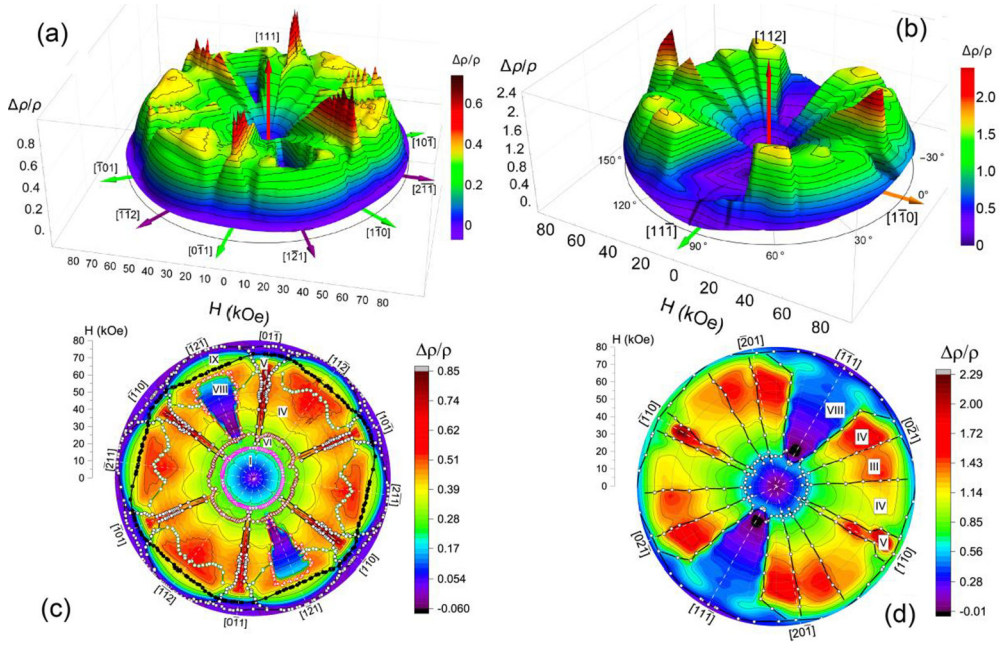

FIG. 5. Magnetoresistance $\Delta\rho/\rho = f(H, \varphi)$ of the $Ho^{11}B_{12}$ in cylindrical coordinates for the current direction $I\|[111]$ (a) and $I\|[112]$ (b) and its projection onto (111) and (112) planes (c) and (d), respectively at $T = 2.1$ K. Roman numerals show different magnetic phases in the AF state.

with a radius of $H \sim 20$ kOe; (2) the area in the wide neighborhood of [100] direction where the maximum MR values are achieved; (3) the region with the minimum MR values around [111] direction; (4) the zone with positive MR that is symmetrical concerning the direction of dynamic charge stripes $\boldsymbol{H}\|[110]$.

Note, that the edges of these plane H-φ diagrams [Figs. 4(c), 4(d), 5(c), and 5(d)] provide important information related to the arrangement of four different sections of the *spherical H-φ-θ (*3D*) magnetic phase diagram* in cases when the $\boldsymbol{H}$ vector lies in planes perpendicular to the measuring current axes. Figure 6(a) shows the combined H-φ planes for measuring current directions $\boldsymbol{I}\|[100]$ and $\boldsymbol{I}\|[1\bar{1}0]$ [see Figs. 4(c)–4(d)] for $Ho^{11}B_{12}$ at T = 2.1 K and presents also schematic views of the main regions [phases I, III, IV, and VIII in Figs. 4(c)–4(d)] in the 3D H-φ-θ space constructed with the help of two more sets of experimental data (iii) $\boldsymbol{I}\|[111]$ and (iv) $\boldsymbol{I}\|[112]$ [see Figs. 5(c)and 5(d)]. Since these four H-φ planes for various measuring current directions were obtained on different samples cut from one single crystal ($\boldsymbol{n}\|[110]$ plate) of $Ho^{11}B_{12}$, we can compare rather the behavior of MR than the absolute values of MR amplitude. However, it can be seen that the phase boundaries obtained from these experiments with different rotational axes coincide very well. One more schematic view (the projection on the spherical surface) of three basic high-field phases (III, IV, and VIII) is shown in Fig. 6(b). It is worth noting that these three segments corresponding to three different types of magnetic phases [III, IV, and VIII, see Figs. 4, 5, and 6(a)] in combination with the low-field spherical area [phase I, Figs. 4(c), 4(d), 5(c), 5(d), and 6(a)] fill almost completely the space inside the AF region in the 3D H-φ-θ phase diagram. The dashed lines in Fig. 6(b) indicate the angular $\varphi = (\boldsymbol{n}, \boldsymbol{H})$ trajectories in these four experiments: (i) A-B-A corresponds to rotation from $\boldsymbol{H}\|[010]$ to $\boldsymbol{H}\|[001]$ [see Fig. 4(c)]; (ii) A-C-B corresponds to rotation from $\boldsymbol{H}\|[001]$ to $\boldsymbol{H}\|[110]$ [see Fig. 4(d)]; (iii) B-c-B corresponds to rotation from $\boldsymbol{H}\|[011]$ to $\boldsymbol{H}\|[110]$ [see Fig. 5(c)], and (iv) B-a-b-C corresponds to rotation from $\boldsymbol{H}\|[011]$ to $\boldsymbol{H}\|[111]$ [see Fig. 5(d)]. Thus, it is obvious that despite the partial similarity of the borders in H-T phase diagrams of

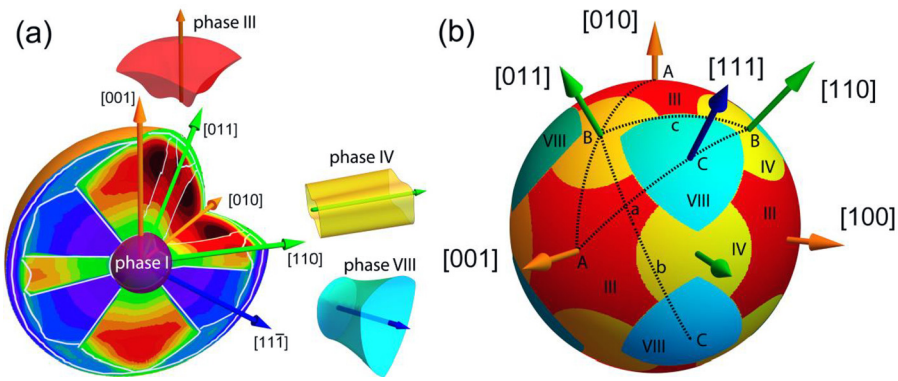

FIG. 6. (a) H-φ phase diagrams of HoB_{12} for current directions $I\|[100]$ and $I\|[1\bar{1}0]$ combined into one 3*D* H-φ-θ phase diagram. Purple, cyan, yellow, and red shapes show four key segments (phases I, VIII, IV, and III, correspondingly) in the center and in the vicinity of principal axes that determine the anisotropy of the phase diagram. (b) Schematic view of the projection on the spherical surface at $H \sim 60$ kOe of three basic high-field phases (III, IV, and VIII) in the H-φ-θ phase diagram. The dashed lines in panel (b) indicate the trajectories of angle φ variation in four experiments with sample rotation (see text for details).

$Ho^{11}B_{12}$ for various magnetic field directions [Figs. 1(c)–1(e)], the set of phases in three principal directions is almost completely different. Such a pronounced anisotropy of charge carriers scattering and of the magnetic phase diagram should be associated with the interaction of the external magnetic field with the dynamic charge stripe structure in $Ho^{11}B_{12}$. Note that the observed effects cannot be related to the Fermi surface (FS) topology of the RB_{12} compound. The main sheet of the FS of RB_{12} has the form of a "monster" [20–22] with open orbit directions along the ⟨111⟩ axis. Despite the highly anisotropic hole sheet, the electron FS sheet is quite isotropic. Moreover, taking into account the small enough mean free path of electrons/holes, the low-field regime $\mu_H H \ll 1$ of charge transport is valid even in the nonmagnetic reference compound LuB_{12}, so it seems natural that the obtained complex magnetic phase diagram cannot be associated with the FS anisotropy. Besides, if considering the stripes as the main factor to be responsible for a strong renormalization of the indirect RKKY exchange interaction, one needs to expect a huge suppression of the nearest neighbor exchange (J_1) in this model AF metal. Indeed, the long-range RKKY magnetic interaction between localized magnetic moments of d, or f orbitals in metals is transmitted by spin density oscillations of conduction electrons [see Fig. 1(b)], and these are suppressed dramatically in the presence of dynamic charge stripes (fast quantum vibrations of the nonequilibrium charge density with a frequency of ∼200 GHz [23]) directed along the ⟨110⟩ axes. Thus, the stripe direction corresponds to the location of neighboring magnetic ions [Figs. 1(a), the Ho-Ho distance is about 5.3 Å] and destroys totally the nearest neighbor RKKY interaction (Fig. 1).

To support these ARM experimental findings an independent estimate of the nearest neighbor (J_1) and next-nearest neighbor (J_2) interactions was undertaken [24]. With this purpose, the magnon dispersion data in HoB_{12} [19] were compared with the results of classical Monte Carlo (MC) simulation. The full version of the MC study will be published elsewhere [25]. It is worth noting here that the deduced very small J_1 value detected in the MC simulations confirm the suppression of RKKY exchange interaction between the nearest Ho ions in the model antiferromagnet.

III. CONCLUSION

In summary, the model SCES $Ho^{11}B_{12}$ compound with incommensurate AF structure, cooperative Jahn-Teller instability of boron network, and dynamic charge stripes was studied in detail by ARM measurements at liquid helium temperature. For this nonequilibrium AF metal, strongly anisotropic polar H-φ-θ magnetic phase diagrams were reconstructed. It is shown that they consist of four basic sectors: a spherical low-field region and three variously complicated cone-shaped segments detected in the vicinity of principal directions: (a) along ($\boldsymbol{H}\|[110]$) and (b) transverse to ($\boldsymbol{H}\|[001]$) the dynamic charge stripes, and (c) parallel to the axis of magnetic structure ($\boldsymbol{H}\|[111]$) in the *fcc* lattice. We argue that *the strong anisotropy* both of the phase diagram and the charge transport *is a fingerprint of the electron instability* related to the formation of a filamentary structure (fluctuating charge carrier channels along [110] direction) of nonequilibrium electrons. As a result, *the indirect* RKKY *exchange interaction* between the nearest neighbor magnetic ions located at the distance of ∼5.3 Å in ⟨110⟩ directions *is dramatically destroyed providing magnetic symmetry lowering* and leading to field-angular phase diagrams with a huge number of magnetic phases and phase transitions.

ACKNOWLEDGMENTS

This work was supported by the Russian Science Foundation, Project No. 17-12-01426 and Russian Foundation for Basic Research, Project No. 18-02-01152 and was performed using the equipment of the Shared Facility Center for Studies of HTS and Other Strongly Correlated Materials, Lebedev Physical Institute, the Russian Academy of Sciences, and the Center of Excellence, Slovak Academy of Sciences. The work of K.F. and S.G. is supported by the Slovak agencies APVV (Grant No. 17–0020) and DAAD-SAS (Grant No. 57452699). The authors are grateful to V. Krasnorussky for experimental assistance.

[1] E. Dagotto, Complexity in strongly correlated electronic systems, Science **309**, 257 (2005).

[2] J. Mitchell, D. Argyriou, A. Berger, K. Gray, R. Osborn, and U. Welp, Spin, charge, and lattice states in layered magnetoresistive oxides, J. Phys. Chem. B **105**, 10731 (2001).

[3] E. Dagotto, *Nanoscale Phase Separation and Colossal Magnetoresistance* (Springer, Berlin, 2003).

[4] B. Keimer, S. A. Kivelson, M. R. Norman, S. Uchida, and J. Zaanen, From quantum matter to high-temperature superconductivity in copper oxides, Nature (London) **518**, 179 (2015).

[5] E. Berg, E. Fradkin, S. A. Kivelson, and J. M. Tranquada, Striped superconductors: how spin, charge and superconducting orders intertwine in the cuprates, New J. Phys. **11**, 115004 (2009).

[6] S. Sachdev and B. Keimer, Quantum criticality, Phys. Today **64**, 29 (2011).

[7] S. Nakatsuji, V. Dobrosavljević, D. Tanasković, M. Minakata, H. Fukazawa, and Y. Maeno, Mechanism of Hopping Transport in Disordered Mott Insulators, Phys. Rev. Lett. **93**, 146401 (2004).

[8] T. Sasaki, N. Yoneyama, A. Matsuyama, and N. Kobayashi, Magnetic and electronic phase diagram and superconductivity in the organic superconductors $\kappa-$aET) 2 X, Phys. Rev. B **65**, 060505(R) (2002).

[9] R. M. Fernandes, A. V. Chubukov, and J. Schmalian, What drives nematic order in iron-based superconductors?, Nat. Phys. **10**, 97 (2014).

[10] J. Lee, F. Schmitt, R. Moore, S. Johnston, Y.-T. Cui, W. Li, M. Yi, Z. Liu, M. Hashimoto, and Y. Zhang, Interfacial mode

coupling as the origin of the enhancement of T c in FeSe films on $SrTiO_3$, Nature (London) **515**, 245 (2014).

[11] S. Demishev, V. Krasnorussky, A. Bogach, V. Voronov, N. Y. Shitsevalova, V. Filipov, V. Glushkov, and N. Sluchanko, Electron nematic effect induced by magnetic field in antiferroquadrupole phase of CeB_6, Sci. Rep.-UK **7**, 1 (2017).

[12] N. Sluchanko, A. Bogach, N. Bolotina, V. Glushkov, S. Demishev, A. Dudka, V. Krasnorussky, O. Khrykina, K. Krasikov, and V. Mironov, Rattling mode and symmetry lowering resulting from the instability of the B_12 molecule in LuB_12, Phys. Rev. B **97**, 035150 (2018).

[13] N. B. Bolotina, A. P. Dudka, O. N. Khrykina, V. N. Krasnorussky, N. Y. Shitsevalova, V. B. Filipov, and N. E. Sluchanko, The lower symmetry electron-density distribution and the charge transport anisotropy in cubic dodecaboride LuB_{12}, J. Phys.: Condens. Matter **30**, 265402 (2018).

[14] N. Sluchanko, A. Khoroshilov, V. Krasnorussky, A. Bogach, V. Glushkov, S. Demishev, K. Krasikov, N. Y. Shitsevalova, and V. Filippov, Magnetic phase transitions and the anisotropy of charge carrier scattering in antiferromagnetic metal $Ho_{0.5}Lu_{0.5}B_{12}$ with dynamic charge stripes, Bull. Russ. Acad. Sci.: Phys. **83**, 853 (2019).

[15] A. L. Khoroshilov, V. N. Krasnorussky, K. M. Krasikov, A. V. Bogach, V. V. Glushkov, S. V. Demishev, N. A. Samarin, V. V. Voronov, N. Y. Shitsevalova, V. B. Filipov, S. Gabani, K. Flachbart, K. Siemensmeyer, S. Y. Gavrilkin, and N. E. Sluchanko, Maltese cross anisotropy in $Ho_{0.8}Lu_{0.2}B_{12}$ antiferromagnetic metal with dynamic charge stripes, Phys. Rev. B **99**, 174430 (2019).

[16] A. Khoroshilov, V. Krasnorussky, A. Bogach, V. Glushkov, S. Demishev, A. Levchenko, N. Shitsevalova, V. Filipov, S. Gabáni, and K. Flachbart, Anisotropy of Magnetoresistance inHoB_{12}, Acta Phys. Pol. A **131**, 976 (2017).

[17] See Supplemental Material at http://link.aps.org/supplemental/10.1103/PhysRevB.102.214435 for detailson Temperature dependences of the specific heat for **H**‖[100], **H**‖[110], and **H**‖[111] (Fig. S1), magnetization dependences (Figs. S2a–S2c) and *dM/dH* derivatives (Figs. S2d–S2f) versus magnetic field for **H**‖[100], **H**‖[110]and **H**‖[111]directions were used to refine H-T phase diagram [Figs. 1(c)–1(e)]. Magnetic field derivatives of MR (Fig. S3) were used to obtain angular phase boundaries on the H-φ phase diagram [Fig. 4(c)]. Data sets from experiments with sample rotation around current directions (iii) ***I***‖[111] and (iv) ***I***‖[112] (Figs. S4–S7).

[18] A. Kohout, I. Batko, A. Czopnik, K. Flachbart, S. Matas, M. Meissner, Y. Paderno, N. Shitsevalova, and K. Siemensmeyer, Phase diagram and magnetic structure investigation of the fcc antiferromagnet HoB_{12}, Phys. Rev. B **70**, 224416 (2004).

[19] K. Siemensmeyer, K. Habicht, T. Lonkai, S. Mat'as, S. Gabani, N. Shitsevalova, E. Wulf, and K. Flachbart, Magnetic properties of the frustrated fcc - Antiferromagnet HoB_{12} above and below *T* (N), J. Low. Temp. Phys. **146**, 581 (2007).

[20] M. Heinecke, K. Winzer, J. Noffke, H. Kranefeld, H. Grieb, K. Flachbart, and Y. B. Paderno, Quantum oscillations and the Fermi surface of LuB_{12}, Z. Phys. B **98**, 231 (1995).

[21] H. Liu, M. Hartstein, G. J. Wallace, A. J. Davies, M. C. Hatnean, M. D. Johannes, N. Shitsevalova, G. Balakrishnan, and S. E. Sebastian, Fermi surfaces in Kondo insulators, J. Phys.: Condens. Matter **30**, 16LT01 (2018).

[22] V. A. Gasparov, I. Sheikin, F. Levy, J. Teyssier, and G. Santi, Study of the Fermi Surface of ZrB_{12} Using the de Haas-van Alphen Effect, Phys. Rev. Lett. **101**, 097006 (2008).

[23] N. Sluchanko, A. Azarevich, A. Bogach, N. Bolotina, V. Glushkov, S. Demishev, A. Dudka, O. Khrykina, V. Filipov, and N. Y. Shitsevalova, Observation of dynamic charge stripes in $Tm_{0.19}Yb_{0.81}B_{12}$ at the metal–insulator transition, J. Phys.: Condens. Matter **31**, 065604 (2018).

[24] K. Krasikov, V. Glushkov, S. Demishev, A. Khoroshilov, A. Bogach, V. Voronov, N. Shitsevalova, V. Filipov, S. Gabani, K. Flachbart, K. Siemensmeyer, and N. Sluchanko, Suppression of indirect exchange and symmetry breaking in antiferromagnetic metal with dynamic charge stripes arXiv:2004.10421.

[25] T. Huberman, D. Tennant, and K. Siemensmeyer *et al.* (unpublished).